Accessing the Intrinsic Spin Transport in a Topological Insulator by Controlling the Crossover of Bulk-to-Surface Conductance

Wonhee Ko, Giang D. Nguyen, Hoil Kim, Jun Sung Kim, X.-G. Zhang, and An-Ping Li

Phys. Rev. Lett. **121**, 176801 — Published 24 October 2018

DOI: 10.1103/PhysRevLett.121.176801

Access the intrinsic spin transport in topological insulator by controlling the crossover of bulk-to-surface conductance

Wonhee Ko[1], Giang D. Nguyen[1], Hoil Kim[2,3], Jun Sung Kim[2,3], X.-G. Zhang[4], An-Ping Li[1*]

[1]*Center for Nanophase Materials Sciences, Oak Ridge National Laboratory, Oak Ridge, Tennessee 37831, USA*

[2]*Department of Physics, Pohang University of Science and Technology, Pohang 37673, Korea*

[3]*Center for Artificial Low Dimensional Electronic Systems, Institute for Basic Science, Pohang 37673, Korea*

[4]*Department of Physics and Quantum Theory Project, University of Florida, Gainesville, Florida 32611, USA*

** Email: apli@ornl.gov*

Abstract

We report a method to control contributions of bulk and surface states in topological insulator Bi_2Te_2Se that allows accessing the spin-polarized transport endowed by topological surface states. An intrinsic surface dominant transport is established when cooling the sample to low temperature or reducing the conduction channel length, both achieved *in situ* in the transport measurements with a four-probe scanning tunneling microscope without the need of further tailoring the sample. The topological surface states show characteristic transport behaviors with mobility about an order of magnitude higher than reported before, and a spin polarization approaching theoretically predicted value. Our result demonstrates accessibility to the intrinsic high mobility spin transport of topological surface states, which paves a way to realizing topological spintronic devices.

Topological insulators possess non-trivial topology which results in the topological surface states with massless Dirac fermions and peculiar spin texture, while their bulk states have band gap and behave as insulator [1,2]. The transport through the surface is expected to exhibit superior mobility from prohibited backscattering and spin-polarized current from spin-momentum locking, which makes them a promising material for spintronic applications [3-11]. In realistic experimental conditions, however, there exist bulk carriers from thermal excitation and defect states, which are not topologically protected but contribute to the total conductance [3,4,12]. To achieve the full potential of the topological insulators, bulk carriers need to be suppressed and the surface should be the dominant transport channel.

One common method to suppress bulk carriers in topological insulators is to reduce the thickness of the materials. Thin film of topological insulators based on Bi chalcogenides was fabricated by exfoliating single crystal down to a few layers, or by growing layer-by-layer with molecular beam epitaxy (MBE) [13-16]. Transport measurement on thin films showed strong evidence of conduction through topological surface states, such as finite conductivity from the surface at low temperature despite insulating bulk [14-17]. A significant enhancement in mobility was observed for the devices fabricated from the thin films [14-18], and charge-current induced spin polarization was detected by reducing film thickness [3-7]. However, the measured values of mobility and spin polarization are far short of theoretical prediction [19-21]. Despite the great amount of effort to enhance the mobility, such as the MBE growth of meticulously designed heterostructure of Bi-based topological insulator, mobility only reached 16,000 $cm^2/(V \cdot s)$ [18]. This is far less than the mobility of materials with similar band structure, like graphene, which shows mobility of 200,000 $cm^2/(V \cdot s)$ [22]. It is uncertain whether the discrepancy reflects an “intrinsic” limit in application of the topological surface states. For

example, it has been speculated that thin film structure has a disadvantage because the proximity of top and bottom surface states in the thin film makes two surface states screen each other and even hybridize to change the topology of the surface states [13,17]. Moreover, exfoliation of single crystal inevitably accompanies exposure to atmospheric gas or polymers, and MBE growth of thin film can also introduce domains with strains and defects [14,23-25], which all hinders the access of the intrinsic properties of the surface states. Not to mention that *ex situ* transport measurement of lithographically fabricated devices suffers from severe contaminations of the surface. To avoid the degradation of surface states by extrinsic factors, it is necessary to explore alternative routes to access intrinsic surface conduction in high-quality crystal samples.

In situ transport measurement with a four-probe scanning tunneling microscope (4P-STM) is a promising method to study the pristine surface of topological insulators. *First*, the crystalline sample can be cleaved in the ultra-high vacuum (UHV) chamber and measured at variable temperatures with four STM probes as movable electrodes [26,27]. *Second*, bulk and surface conductance can be differentiated with 4P-STM by measuring four-probe resistance with variable probe-spacing [28], which allows extracting the bulk and surface conductivity separately even when bulk and surface conduction occur simultaneously. *Third*, utilizing ferromagnetic probe, the measurements allow detection of spin polarization of carriers when surface conduction is dominate [11]. However, the ratio between the bulk and surface conduction is a function of external parameters, such as temperature and length of conduction channel, and the intrinsic conductance of surface states can only be revealed when the crossover of bulk-to-surface conductance can be controlled.

In this Letter, we study the intrinsic surface conductance of topological insulators by using 4P-STM spectroscopy to tune the crossover of bulk-to-surface conductance, and report an

extremely high carrier mobility and large spin-polarization of surface conductance in Bi_2Te_2Se. By controlling the probe-spacing and temperature, we realize almost 100 % surface conductance on the single crystal of Bi_2Te_2Se, a topological insulator with bulk-insulating conductivity [2,29-32]. The observed transport properties of topological surface states exhibit a carrier mobility of 61,000 $cm^2/(V \cdot s)$ and current-induced spin polarization of 72%, revealing a nearly scattering-free transport. The results show that 4P-STM is an ideal tool to access surface dominant conduction and observe topological transport phenomena without altering the sample.

Single crystal of Bi_2Te_2Se was grown by the self-flux method following the previously reported procedure [29], and *ex situ* transport measurement was done with physical property measurements system to confirm the insulating bulk behavior (see details in Supplementary Material [33]). For multiprobe STM/transport measurement, we utilized cryogenic 4P-STM that operates at UHV condition ($< 8 \times 10^{-10}$ torr) [27,34]. Single probe STM/STS was performed both by 4P-STM and variable temperature STM. Etched tungsten tips were used for STM/transport measurement, except for spin-polarized measurements where etched nickel tips were used [11,35]. Samples were cleaved in UHV and characterized within two days except for intentionally "aged" samples. Samples were thicker than 500 μm to prevent any interaction between the top and the bottom surfaces and leakage current to the sample holder. A source-measure unit was utilized to measure four probe contact *I*-*V* curves with 4P-STM, and conventional lock-in technique was used to measure tunneling d*I*/d*V* spectra with the single tip.

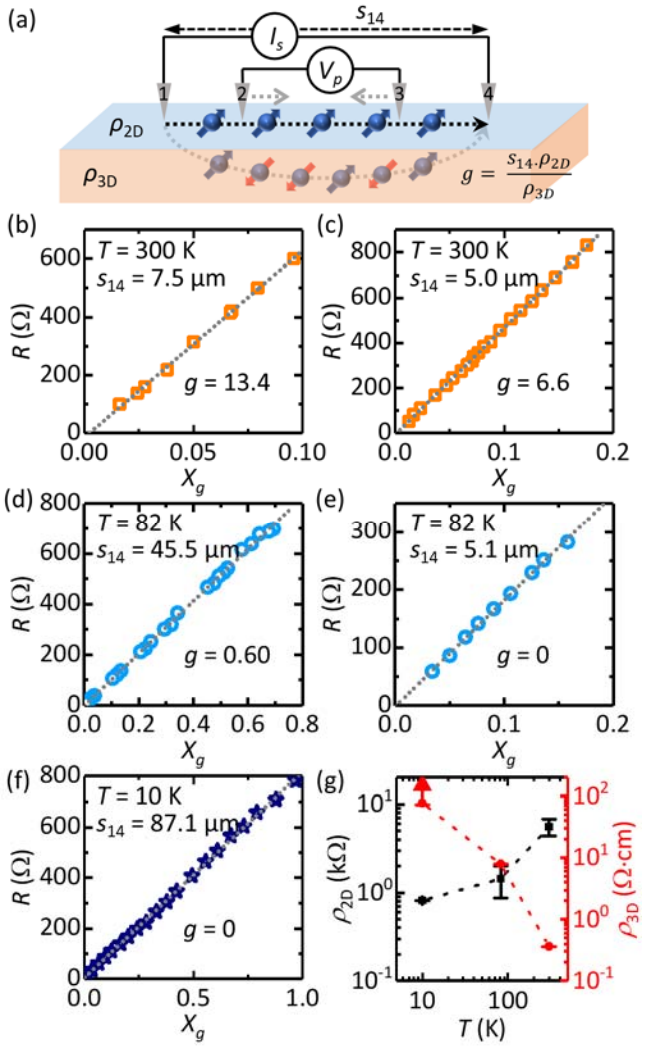

FIG. 1. (a) Schematics of electron transport through bulk and surface in a topological insulator, and transport measurements by variable probe-spacing spectroscopy with 4P-STM. (b)-(f) Resistance vs. X_g measured by variable probe-spacing spectroscopy at various temperature and probe spacing. Each graph is plotted with the g value that produces the best linear fit. (g) Surface and bulk resistivity extracted from variable probe-spacing spectroscopy. At 10 K, ρ_{3D} was not extractable, and so the lower limit is marked by an arrow.

Variable probe-spacing spectroscopy is utilized to detect bulk and surface contribution to the transport. Figure 1(a) shows the measurement scheme, where four STM tips are placed

collinearly and directly contacting the sample surface. Two inner voltage probes are moved step-by-step toward each other while two outer source probes are fixed. Bulk and surface transport can be differentiated because the surface states are confined to extremely thin area (estimated to be less than 5 nm from its wavefunction penetration depth into the bulk [13,36]) and can be treated as a 2D sheet, while 3D bulk states are distributed in depth comparable to the source probe spacing (> 1μm). Bulk and surface are modeled as 3D and 2D conduction channels interconnected at all points on the surface, where the potential distribution $V(\vec{r})$ between the two source probes is derived as [28],

$$V(\vec{r}) = \rho_{2D} \cdot \frac{I}{2\pi} \cdot \ln\left[\frac{\left(\frac{\rho_{2D}}{\rho_{3D}} + \frac{1}{|\vec{r}-\vec{r_1}|}\right)}{\left(\frac{\rho_{2D}}{\rho_{3D}} + \frac{1}{|\vec{r}-\vec{r_4}|}\right)}\right], \qquad (1)$$

where I is the amount of the current, ρ_{2D} and ρ_{3D} are surface and bulk resistivity, and $\vec{r_1}$ and $\vec{r_4}$ are the positions of two source probes. Denoting distances between the tip i and j as s_{ij}, the resistance between the voltage probes R can be expressed as

$$R = \frac{\Delta V}{I} = \rho_{2D} \cdot \frac{1}{2\pi} \ln\left[\frac{\left(g+\frac{s_{14}}{s_{12}}\right)\left(g+\frac{s_{14}}{s_{34}}\right)}{\left(g+\frac{s_{14}}{s_{13}}\right)\left(g+\frac{s_{14}}{s_{24}}\right)}\right], \qquad (2)$$

where $g \equiv \rho_{2D}/\rho_{3D} \times s_{14}$. Here, g is a dimensionless parameter representing the ratio between the surface and bulk conductance, which approaches zero for surface dominant transport but infinite for bulk dominant transport. We define X_g as

$$X_g = \frac{1}{2\pi} \ln\left[\frac{\left(g+\frac{s_{14}}{s_{12}}\right)\left(g+\frac{s_{14}}{s_{34}}\right)}{\left(g+\frac{s_{14}}{s_{13}}\right)\left(g+\frac{s_{14}}{s_{24}}\right)}\right], \qquad (3)$$

then $R = \rho_{2D} \cdot X_g$, i.e., R is linearly proportional to X_g only if the correct value is used for g. By varying g until R-X_g curve gives the best linear fit, we can extract ρ_{2D} and ρ_{3D} from the slope and g, respectively, as $\rho_{2D} = 2\pi \cdot R/X_g$ and $\rho_{3D} = \rho_{2D}\, s_{14}/g$.

Figure 1(b)-(f) shows R-X_g curves taken at various temperature and probe spacing, where g is obtained as the value that gives the best linear fit. When the temperature is fixed, smaller probe spacing always resulted in smaller g [e.g., compare Fig. 1(b) and 1(c), or Fig. 1(d) and 1(e)]. At 300 K, bulk resistivity is small and surface resistivity is large so bulk conduction is always dominant. When temperature is lowered to 82 K, bulk resistivity increases while surface resistivity decreases and surface dominant conduction becomes achievable at small probe spacing. By controlling probe spacing at 82 K, g can be changed from 13.35 to 0, corresponding to a change of surface contribution to the conductivity from 7 % to 100 %. At 10 K, bulk resistivity is so high that the surface conduction is always dominant even at macroscopic length scale [Fig. 1(f)]. The behavior also matches with the *ex situ* transport measurement of resistivity, where ρ increases with decreasing temperature due to the bulk contribution but saturates at low temperature because of the surface [29,32,33].

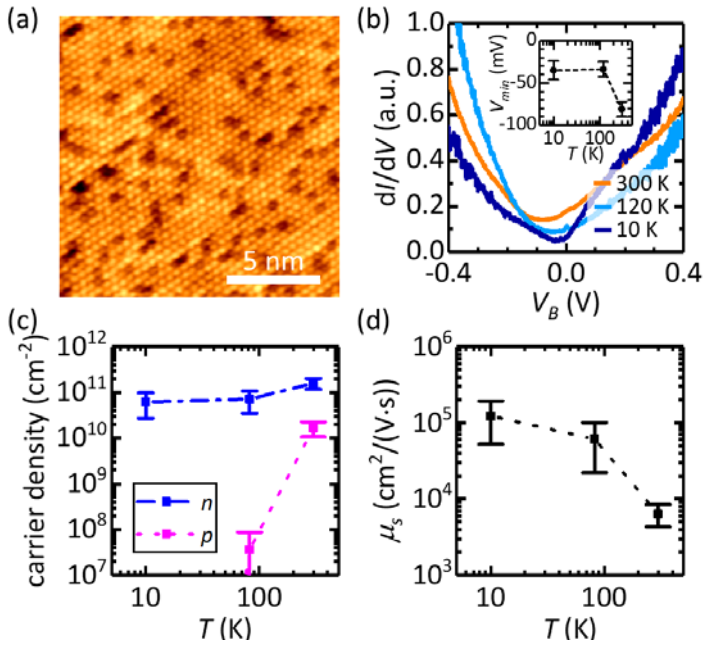

FIG. 2. (a) Topographic image with atomic resolution of Bi_2Te_2Se (V_B = -0.5 V, I = 0.9 nA). (b) dI/dV spectra of Bi_2Te_2Se taken at various temperature (lock-in amplifier modulation voltage V_{mod} = 20 mV for T = 300 K and V_{mod} = 5 mV for others, and modulation frequency f_{mod} = 1 kHz for all temperature). The inset shows the bias voltage of minimum dI/dV extracted from the spectra. (c),(d) Temperature dependence of surface carrier density and surface mobility, respectively.

We now examine the surface carrier density and mobility. We first performed scanning tunneling spectroscopy (STS) to probe the density of states on the surface by placing single STM tip in the tunneling regime. STM topographic image confirms that the surface is atomically clean [Fig. 2(a)]. Note, dark atomic sized regions in the topographic image are not external impurities, but the Te atoms substituting the Se atoms at the surface layer as studied before [37,38]. Figure 2(b) shows tunneling dI/dV spectra taken at various temperatures. Each spectrum is an average of ten spectra taken on different points over the 30 nm long line, where there was no significant change with the position. The dI/dV curves have a typical V-shape of the Bi-based topological

insulators, where the minimum point V_{min} corresponds to the Dirac point E_D [11,39]. At a temperature of 120 K and below, the V_{min} has a nearly fixed value of -35 mV, namely, $E_D - E_F = eV_{min}$ = -35 ± 10 meV, where E_F is Fermi level and e is the electron charge (for convenience, we set E_F = 0). However, at room temperature, V_{min} shifts to -80 mV. As shown in the variable probe-spacing spectroscopy, the bulk conductance is dominant at room temperature. Therefore, the tunneling dI/dV does not reflect the surface but the bulk density of states (details in Supplementary Material [33]). Given the small band gap of the Bi_2Te_2Se (~300 meV [31,39]), a large number of bulk carriers from thermal excitation contributes to the conductance in this regime. The observation of V_{min} = -80 mV indicates that bulk electron density is much larger than bulk hole density, i.e., the bulk is n-type semiconductor (Supplementary Material [33]).

Surface carrier density and surface mobility can be derived from E_D with respect to the E_F, considering that the surface states of Bi_2Te_2Se accommodate massless Dirac fermions whose band dispersion can be written as $E = \hbar v_F k + E_D$, where v_F is Fermi velocity (~ 6×10^5 m/s for Bi_2Te_2Se [11,28,31]). Thus, electron density n and hole density p are derived as

$$n = \frac{1}{2\pi}\left(\frac{k_B T}{\hbar v_F}\right)^2 \int_0^\infty \frac{u}{1+e^{u-\eta}} \cdot du, \qquad (4)$$

$$p = \frac{1}{2\pi}\left(\frac{k_B T}{\hbar v_F}\right)^2 \int_0^\infty \frac{u}{1+e^{u+\eta}} \cdot du, \qquad (5)$$

where $u = E/k_B T$, and $\eta = -E_D/k_B T$ [40]. The surface mobility μ_s are calculated as $\mu_s = \frac{1}{e(n+p)\rho_{2D}}$. The derived surface carrier density and surface mobility are plotted in Fig. 2(c) and 2(d) as a function of temperature, respectively. An enhancement of μ_s is seen at low temperature and μ_s becomes larger than 61,000 $cm^2/(V \cdot s)$ below 82 K and reach 120,000 $cm^2/(V \cdot s)$ at 10 K, which is about an order of magnitude higher than the highest mobility (16,000 $cm^2/(V \cdot s)$ at 1.5 K)

previously reported for thin film of Bi-based topological insulators [18]. Even considering the variations of v_F value and Dirac point, by using the smallest $v_F \sim 4.5 \times 10^5$ m/s reported in literature [29,41] and the lowest E_D of -45 meV measured in our sample, we still find a lower limit of the surface mobility of 30,000 $cm^2/(V \cdot s)$ at 10 K.

The lower limit of surface mobility at 10 K is more than 400 times larger than that of the same bulk sample measured *ex situ* [33]. The surface mobility is also an order of magnitude larger than previously reported values from *ex situ* transport measurements on the same material [29,32]. Such high mobility represents the intrinsic property of the surface as the sample surface is atomically clean and the measurement is performed *in situ* in the UHV chamber. As a comparison experiment, we left the sample in the UHV chamber for a week to allow the residual gas adsorption on the surface. Such an "aging" process in the UHV has been reported to increase doping and shift E_D to more negative value [28,42,43]. Indeed, a repeated measurement at 82 K shows that E_D changes from -35 ± 10 meV of the freshly cleaved surface to -160 ± 30 meV on the "aged" surface (further details see Fig. S2 in Supplementary Material [33]). Meanwhile, the surface mobility decreases from 61,000 $cm^2/(V \cdot s)$ to 8,000 $cm^2/(V \cdot s)$, which indicates significant degradation of surface conduction by increased impurity scattering. The observation confirms the importance of surface cleanness for achieving intrinsic high mobility of surface carriers.

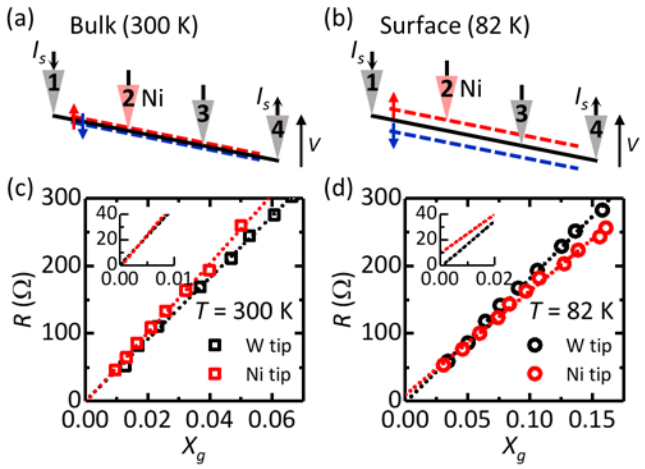

FIG. 3. (a), (b) Schematic of spin-dependent potential measurement with a ferromagnetic tip for bulk and surface conduction, respectively. The spin-dependent potential is drawn in red and blue dotted line, which splits from the average potential (black solid line) for surface conduction, but not for the bulk. (c) Comparison of variable probe-spacing spectroscopy with one voltage probe from either magnetic (Ni) or non-magnetic (W) tip at room temperature (s_{14} = 5.0 μm and g = 6.6 for the W tip data, and s_{14} = 6.2 μm and g = 9.6 for the Ni tip data). Inset shows the zoomed graph around X_g = 0. (d) Comparison of variable probe-spacing measurement with one voltage probe from either magnetic (Ni) or non-magnetic (W) tip at 82 K (s_{14} = 5.1 μm and g = 0 for W tip data, and s_{14} = 5.3 μm and g = 0 for Ni tip data). Inset shows the zoomed graph around X_g = 0.

In the surface dominant conductance regime, a spin-polarized transport is expected. Topological surface states possess unique spin texture from spin-momentum locking, and the current through the surface states creates a potential difference for different spin directions, while bulk states are spin-degenerate and exhibit no spin-dependent potential [20,21]. By using a spin-polarized 4P-STM, we can measure the surface potential difference between a ferromagnetic probe and non-magnetic probe at the same sample location, and the potential difference corresponds to the spin accumulation induced by spin-polarized current [11]. As schematically shown in Fig. 3(a) and 3(b), spin-dependent conductance is measured with variable probe-

spacing spectroscopy when one of the voltage probes is substituted by a ferromagnetic (Ni) probe. To remove any possible thermoelectric effect between the Ni and W probes, we assured that all tips and sample are at thermal equilibrium with the cryostat where the temperature gradient is less than 1 K [11,34,44,45]. By following the measurement procedure reported recently [11], we obtain a similar R-X_g curve as shown in Fig. 1, but now with additional resistance arising from the imbalance of spin-dependent chemical potentials on the surface. A ferromagnetic probe will follow the spin-dependent potential profile according to its magnetization (red or blue dotted line in Fig. 3(a) and 3(b)) while non-magnetic probe will follow the spin-averaged potential profile (black solid line in Fig. 3(a) and 3(b)). When X_g approaches zero, namely the distance of magnetic and non-magnetic voltage probes approaches zero, the residue resistance comes from the potential difference between the spin-polarized and spin-averaged channels, which appears as a nonzero R offset in R-X_g curve. Figure 3(c) and 3(d) shows the variable probe-spacing spectroscopy performed with and without ferromagnetic tip, at bulk and surface dominant regimes, respectively. Inset of Fig. 3(c) and 3(d) shows that nonzero offset only occurs when surface dominant conduction is achieved at 82 K. Defining $R_s \equiv R(X_g = 0)$, the linear fitting in Fig. 3(d) for Ni tip data results in R_s = 9.2 ± 3.4 Ω, which can be converted to the spin-polarization of the current as

$$R_s = p \cdot \frac{P_{FM}}{\sqrt{2}} \cdot \frac{h}{{q_e}^2} \frac{1}{2\pi k_F} \left(\frac{1}{s_{12}} + \frac{1}{s_{24}} \right), \qquad (6)$$

where p is the spin polarization of current, P_{FM} is the effective spin sensitivity of Ni tip, and k_F is the Fermi wave vector [11]. Using P_{FM} = 0.5 and $k_F = E_D/(\hbar v_F)$, we estimate p = 72 %. Meanwhile, the linear fitting in Fig. 3(c) for Ni tip data results in R_s = -1.7 ± 3.5 Ω, indicating that there is no detectable spin-dependent potential when bulk conduction is dominant.

The appearance of spin-dependent potential only for surface dominant conduction confirms that the spin polarization originates from the intrinsic spin texture of topological surface states but not from bulk-related or other extrinsic origins [3-7,46]. The measured value of *p* here is larger than most of the previously reported values from *ex situ* transport measurements, and comparable to the theoretical limit for topological surface states [20,21]. Thus, by focusing on a surface dominant conduction regime, we can access the intrinsic transport of topologically protected surface states in topological insulators.

In summary, by performing *in situ* measurement with 4P-STM and controlling the crossover of bulk-to-surface conduction, we have revealed the intrinsic transport behaviors of topological surface states in bulk-insulating topological insulator Bi_2Te_2Se that have been inaccessible to conventional *ex situ* transport measurement. The surface contribution to the conductivity has been tuned from 7 % to 100 % by changing the temperature and the length of conduction channel. In the surface dominate conductance regime, we have observed the highest reported mobility and a spin-polarization of current approaching the theoretically predicted value. Superior intrinsic spin transport of the topological surface states implies that the current performance of topological insulator devices is not limited by the intrinsic properties of the surface states, but by the external conditions such as device geometry and surface contamination [12,14-17]. Of crucial importance includes reducing the conduction channel length and preventing the surface from unintentional doping, which should be achievable with the recent development of lithography techniques and capping of topological insulator with atomically precise interface [18]. The extremely high mobility would be achievable, whose significance can be invoked from the isotropic mobility formula for Dirac electrons [47], $\mu = \frac{ev_F\ell}{2|E_F - E_D|}$, where ℓ is the carrier scattering mean-free-path. Using the measured values for the mobility at 10 K, we

find the mean-free-path $\ell = 1.4$ μm. Therefore, it indicates that the completely scattering-free spin transport through topological surface states would be possible at micrometer scale. This would be observable with 4P-STM because the recent development of multiprobe technique, such as scanning tunneling potentiometry, enables nanoscopic mapping of conductance especially useful for probing local variations of conductance [23-25,45,48-50].

Acknowledgements

This research was conducted at the Center for Nanophase Materials Sciences, which is a DOE Office of Science User Facility. The crystal growth and characterization at POSTECH was supported by the Institute for Basic Science (IBS) through the Center for Artificial Low Dimensional Electronic Systems (no. IBS-R014-D1), and by the National Research Foundation (NRF) of Korea through the SRC (no. 2011-0030785) and the Max Planck-POSTECH Center for Complex Phase Materials in Korea (MPK) (no. 2016K1A4A4A01922028). The theory effort at Florida was supported by NSF DMREF CHE-1534401.

[1] C. L. Kane and E. J. Mele, Phys. Rev. Lett. **95**, 226801 (2005).
[2] L. Fu, C. L. Kane, and E. J. Mele, Phys. Rev. Lett. **98**, 106803 (2007).
[3] Y. Ando *et al.*, Nano Lett. **14**, 6226 (2014).
[4] C. H. Li, O. M. J. Van't Erve, J. T. Robinson, Y. Liu, L. Li, and B. T. Jonker, Nat. Nanotechnol. **9**, 218 (2014).
[5] A. Dankert, J. Geurs, M. V. Kamalakar, S. Charpentier, and S. P. Dash, Nano Lett. **15**, 7976 (2015).
[6] J. Tian, I. Miotkowski, S. Hong, and Y. P. Chen, Sci. Rep. **5**, 14293 (2015).
[7] J. S. Lee, A. Richardella, D. R. Hickey, K. A. Mkhoyan, and N. Samarth, Phys. Rev. B **92**, 155312 (2015).
[8] A. R. Mellnik *et al.*, Nature **511**, 449 (2014).
[9] Y. Shiomi, K. Nomura, Y. Kajiwara, K. Eto, M. Novak, K. Segawa, Y. Ando, and E. Saitoh, Phys. Rev. Lett. **113**, 196601 (2014).
[10] K. Kondou, R. Yoshimi, A. Tsukazaki, Y. Fukuma, J. Matsuno, K. S. Takahashi, M. Kawasaki, Y. Tokura, and Y. Otani, Nat. Phys. **12**, 1027 (2016).
[11] S. M. Hus, X. G. Zhang, G. D. Nguyen, W. Ko, A. P. Baddorf, Y. P. Chen, and A. P. Li, Phys. Rev. Lett. **119**, 137202 (2017).
[12] D. X. Qu, Y. S. Hor, J. Xiong, R. J. Cava, and N. P. Ong, Science **329**, 821 (2010).

[13] Y. Zhang *et al.*, Nat. Phys. **6**, 584 (2010).
[14] J. G. Checkelsky, Y. S. Hor, R. J. Cava, and N. P. Ong, Phys. Rev. Lett. **106**, 196801 (2011).
[15] D. Kim, S. Cho, N. P. Butch, P. Syers, K. Kirshenbaum, S. Adam, J. Paglione, and M. S. Fuhrer, Nat. Phys. **8**, 459 (2012).
[16] A. A. Taskin, S. Sasaki, K. Segawa, and Y. Ando, Phys. Rev. Lett. **109**, 066803 (2012).
[17] Y. Xu *et al.*, Nat. Phys. **10**, 956 (2014).
[18] N. Koirala *et al.*, Nano Lett. **15**, 8245 (2015).
[19] P. Sengupta and E. Bellotti, J. Phys. Condens. Mat. **27**, 405301 (2015).
[20] O. V. Yazyev, J. E. Moore, and S. G. Louie, Phys. Rev. Lett. **105**, 266806 (2010).
[21] S. Hong, V. Diep, S. Datta, and Y. P. Chen, Phys. Rev. B **86**, 085131 (2012).
[22] J. H. Chen, C. Jang, S. Xiao, M. Ishigami, and M. S. Fuhrer, Nat. Nanotechnol. **3**, 206 (2008).
[23] S. Bauer and C. A. Bobisch, Nat. Commun. **7**, 11381 (2016).
[24] F. Lüpke *et al.*, Nat. Commun. **8**, 15704 (2017).
[25] S. Bauer and C. A. Bobisch, J. Phys. Condens. Mat. **29**, 334002 (2017).
[26] T. H. Kim, M. Angst, B. Hu, R. Jin, X. G. Zhang, J. F. Wendelken, E. W. Plummer, and A. P. Li, Proc. Natl. Acad. Sci. USA **107**, 5272 (2010).
[27] A. P. Li, K. W. Clark, X. G. Zhang, and A. P. Baddorf, Adv. Funct. Mater. **23**, 2509 (2013).
[28] C. Durand *et al.*, Nano Lett. **16**, 2213 (2016).
[29] Z. Ren, A. A. Taskin, S. Sasaki, K. Segawa, and Y. Ando, Phys. Rev. B **82**, 241306 (2010).
[30] L. Barreto *et al.*, Nano Lett. **14**, 3755 (2014).
[31] M. Neupane *et al.*, Phys. Rev. B **85**, 235406 (2012).
[32] Z. Ren, A. A. Taskin, S. Sasaki, K. Segawa, and Y. Ando, Phys. Rev. B **84**, 165311 (2011).
[33] See Supplemental Material for detailed methods on sample growth and theoretical calculations, and additional data on aged samples.
[34] T.-H. Kim, Z. Wang, J. F. Wendelken, H. H. Weitering, W. Li, and A.-P. Li, Rev. Sci. Instrum. **78**, 123701 (2007).
[35] J. Park, C. Park, M. Yoon, and A. P. Li, Nano Lett. **17**, 292 (2017).
[36] C. X. Liu, H. Zhang, B. Yan, X. L. Qi, T. Frauenheim, X. Dai, Z. Fang, and S. C. Zhang, Phys. Rev. B **81**, 041307 (2010).
[37] W. Ko *et al.*, Appl. Phys. Lett. **108**, 083109 (2016).
[38] H. Nam *et al.*, J. Phys. Chem. Solids (2017).
[39] M. Nurmamat *et al.*, Phys. Rev. B **88**, 081301 (2013).
[40] T. Fang, A. Konar, H. Xing, and D. Jena, Appl. Phys. Lett. **91**, 092109 (2007).
[41] T. Knispel, W. Jolie, N. Borgwardt, J. Lux, Z. Wang, Y. Ando, A. Rosch, T. Michely, and M. Grüninger, Phys. Rev. B **96**, 195135 (2017).
[42] Y. L. Chen *et al.*, Science **325**, 178 (2009).
[43] A. A. Taskin, Z. Ren, S. Sasaki, K. Segawa, and Y. Ando, Phys. Rev. Lett. **107**, 016801 (2011).
[44] J. Park, G. He, R. M. Feenstra, and A. P. Li, Nano Lett. **13**, 3269 (2013).
[45] K. W. Clark, X. G. Zhang, G. Gu, J. Park, G. He, R. M. Feenstra, and A. P. Li, Phys. Rev. X **4**, 011021 (2014).
[46] P. Li and I. Appelbaum, Phys. Rev. B **93**, 220404 (2016).
[47] C. K. Ullal, J. Shi, and R. Sundararaman, arXiv:1806.10027 (2018).
[48] J. Homoth *et al.*, Nano Lett. **9**, 1588 (2009).
[49] S. H. Ji, J. B. Hannon, R. M. Tromp, V. Perebeinos, J. Tersoff, and F. M. Ross, Nat. Mater. **11**, 114 (2012).
[50] K. W. Clark, X. G. Zhang, I. V. Vlassiouk, G. He, R. M. Feenstra, and A. P. Li, ACS Nano **7**, 7956 (2013).